

Article

The Preparation of g-C₃N₄/CoAl-LDH Nanocomposites and Their Depollution Performances in Cement Mortars under UV-Visible Light

Mengya Huang ^{1,*}, Zhengxian Yang ^{1,*}, Lin Lu ¹, Jiankun Xu ¹, Wencheng Wang ¹ and Can Yang ^{2,*}

¹ Fujian Provincial University Research Center for Advanced Civil Engineering Materials, College of Civil Engineering, Fuzhou University, Fuzhou 350108, China; huangmy027@163.com (M.H.); lulin_edu@163.com (L.L.); jkun15396116557@163.com (J.X.); sdwangwcheng@126.com (W.W.)

² State Key Laboratory of Photocatalysis on Energy and Environment, College of Chemistry, Fuzhou University, Fuzhou 350108, China

* Correspondence: zxyang@fzu.edu.cn (Z.Y.); canyang@fzu.edu.cn (C.Y.)

Abstract: In this study, new organic-inorganic g-C₃N₄/CoAl-LDH nanocomposites were prepared and introduced to fabricate photocatalytic cement mortars by internal mixing, coating, and spraying. The photocatalytic depollution of both g-C₃N₄/CoAl-LDH and cement mortars was assessed by NO_x degradation reaction under UV-visible light irradiation. The study results suggested that the degradation efficiency of g-C₃N₄/CoAl-LDH nanocomposites improved with an increase in g-C₃N₄ content. The g-C₃N₄/CoAl-LDH_{1.5} nanocomposite displayed the highest NO_x degradation capacity, which was about 1.23 and 3.21 times that of pure g-C₃N₄ and CoAl-LDH, respectively. The photocatalytic cement mortars which were all fabricated using different approaches could effectively degrade the target pollutants and exhibited significant compatibility between g-C₃N₄/CoAl-LDH and cementitious substrate. Among them, the coated mortars showed strong resistance to laboratory-simulated wearing and abrasion with a small decrease in degradation rate.

Keywords: g-C₃N₄/CoAl-LDH; heterostructure; cementitious composites; photocatalytic depollution; laboratory-simulated wearing and abrasion



Citation: Huang, M.; Yang, Z.; Lu, L.; Xu, J.; Wang, W.; Yang, C. The Preparation of g-C₃N₄/CoAl-LDH Nanocomposites and Their Depollution Performances in Cement Mortars under UV-Visible Light. *Catalysts* **2022**, *12*, 443. <https://doi.org/10.3390/catal12040443>

Academic Editor: Stéphanie Lambert

Received: 22 March 2022

Accepted: 13 April 2022

Published: 15 April 2022

Publisher's Note: MDPI stays neutral with regard to jurisdictional claims in published maps and institutional affiliations.



Copyright: © 2022 by the authors. Licensee MDPI, Basel, Switzerland. This article is an open access article distributed under the terms and conditions of the Creative Commons Attribution (CC BY) license (<https://creativecommons.org/licenses/by/4.0/>).

1. Introduction

Air pollution has always been a significant concern for human health and ecological environment. Efficient strategies for pollution prevention and control are imminent. Nitrogen oxides NO_x (NO + NO₂) as one of the major pollutants can cause a series of problems, such as photochemical smog, acid rains, and serious respiratory diseases for human [1,2]. In recent years, one of the most promising methods, i.e., photocatalytic technique has played an increasingly essential role in the field of environmental pollution control and received increased attention. For the feasibility of practical applications that introduce photocatalysts into building materials such as cementitious composites [3,4], it is desirable that a photocatalyst can be activated by solar energy for oxidative degradation of air pollutants, providing an efficient way for air purification. So far, TiO₂-based photocatalytic cementitious materials have most commonly been studied in many fields including air purification, sewage treatment, as well as antibacterial and self-cleaning applications. However, there are some inherent disadvantages and problems associating with their practical application: (1) TiO₂ has a wide band gap (3.2 eV) which can only be activated by UV light and has a low utilization rate of solar light [5], (2) TiO₂ does not have satisfactory compatibility with agglomerated cementitious material, which could have a negative effect on the photocatalytic performance [6,7], and (3) the high alkaline environment of cementitious materials probably adversely affect the capacity of photocatalyst [8]. Therefore, endeavors to identify a new stable photocatalytic cementitious material are imperative.

Graphite carbon nitride ($g\text{-C}_3\text{N}_4$) with the graphite-like 2D structure has aroused widespread interest in the field of photocatalysis because of its unique performances, such as a UV-visible light driven band gap (2.7 eV), good thermal stability, low cost, and nontoxicity [9,10]. In recent years, studies have shown that $g\text{-C}_3\text{N}_4$ can be excited by UV-visible light and have found application in hydrogen production, organic pollutant degradation, and air pollution control [9,11,12]. However, due to the short lifetime of photo-induced carriers and inadequate absorption of UV-visible light, pristine $g\text{-C}_3\text{N}_4$ displays relatively low photocatalytic efficiency, which greatly limits its practical application. To improve the properties of $g\text{-C}_3\text{N}_4$, a variety of methods have been proposed, including doping modification [13], precious metal deposition [14], template introduction [15], and semiconductor recombination [16]. Among them, combinations of $g\text{-C}_3\text{N}_4$ with other semiconductors such as TiO_2 [17], SnO_2 [18], ZnCr-LDH [19] have been recognized as the most effective methods to enhance the photocatalytic efficiency.

Layered double hydroxides (LDH) are hydrotalcite-like compounds that contain the main body laminates with metal oxides (M^{2+} and M^{3+}) and adjustable interlayer anions. Due to its unique structure and adjustable band gap, LDH has been widely applied to various photocatalytic applications, such as CO_2 reduction [20], hydrogen generation [21], and photodegradation [22]. In addition, the molecular structure of LDH shares the same characteristics with some cement hydration products and, thus, exhibits good compatibility with cement-based materials as well as chemical stability in its alkaline environment [23–25]. The unique layered structure of LDH can also act as an effective supporting substrate for photocatalysts to avoid direct contact with cementitious materials. This can mitigate the adverse impact of cementitious materials on the photocatalyst and, thus, improve the photocatalytic efficiency [18]. Up to now, many researchers have reported that LDH could act as a co-photocatalyst to improve the inherent shortcomings of other semiconductors due to LDH's suitable potential and narrow band gap [26,27].

The appropriate construction of a $g\text{-C}_3\text{N}_4$ /LDH nanocomposite has the potential to contribute synergistic benefits over that of $g\text{-C}_3\text{N}_4$ and LDH in terms of photocatalytic performances. Research has found that because of the interfacial contact between NiAl-LDH and $g\text{-C}_3\text{N}_4$, the photogenerated charges can separate more efficiently with a low recombination rate [28]. It has been reported that 2D/2D $g\text{-C}_3\text{N}_4\text{-C(N)}/\text{ZnCr-LDH}$ with a higher surface area can increase light harvesting ability and response capacity, and therefore, present a superior photocatalytic performance than individual pure phase [29]. In addition, the chemical properties of $g\text{-C}_3\text{N}_4$ /LDH can be tailored, which makes it suitable for photocatalytic applications in various fields [30,31]. Moreover, according to our investigation, no study has reported for introducing $g\text{-C}_3\text{N}_4$ /LDH into building materials with regard to photocatalytic depollution.

In this work, a group of $g\text{-C}_3\text{N}_4$ /CoAl-LDH nanocomposites were prepared with different contents of $g\text{-C}_3\text{N}_4$. The photocatalytic property and depollution mechanism of the $g\text{-C}_3\text{N}_4$ /CoAl-LDH nanocomposites toward the degradation of NO_x were investigated, while the morphology, microstructure, and photoelectrical properties were characterized by X-ray diffraction (XRD), Fourier transform infrared spectra (FT-IR), field emission scanning electron microscopy coupled with energy-dispersive X-ray spectroscopy (SEM-EDS), UV-VIS diffuse reflectance spectrum (UV-VIS DRS), photoluminescence (PL), electrochemical impedance spectroscopy (EIS), as well as current-time (I-T), and Mott-Schottky (M-S) plots. Furthermore, a series of cement mortars were fabricated with the introduction of $g\text{-C}_3\text{N}_4$ /CoAl-LDH by means of internal mixing, spraying, and coating. The photocatalytic property of the cement mortars was measured by NO_x degradation under UV-visible light, while the durability of the coated mortar was assessed under the laboratory-simulated wearing and abrasion conditions.

2. Results and Discussion

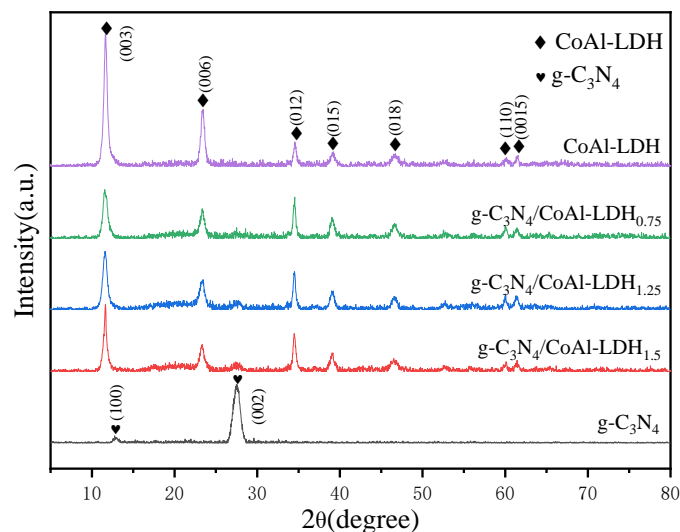
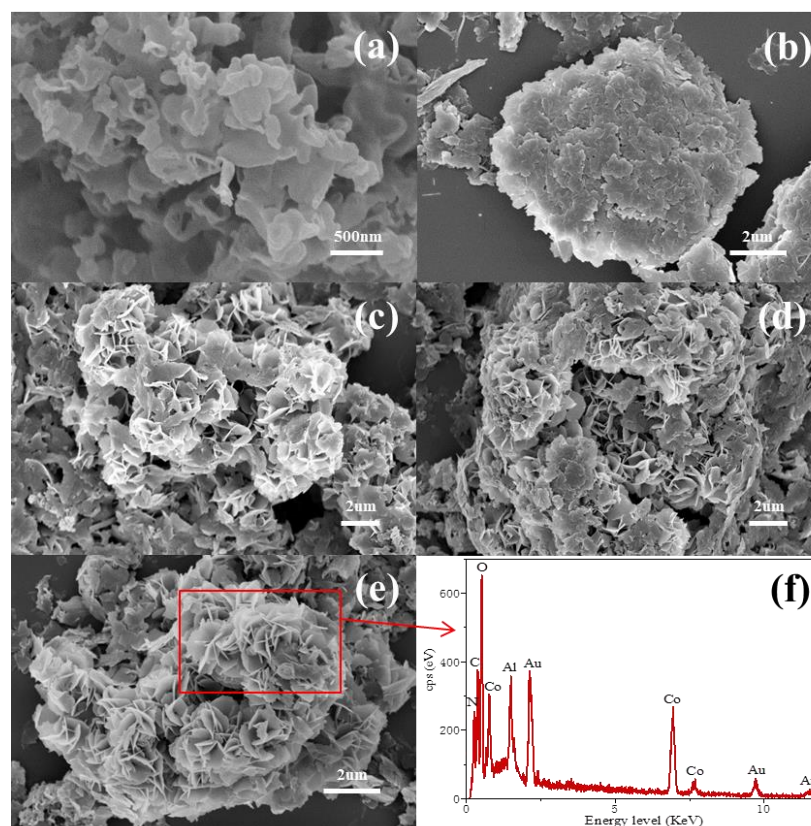
2.1. Characterization of $g\text{-C}_3\text{N}_4$, CoAl-LDH, and the $g\text{-C}_3\text{N}_4/\text{CoAl-LDH}$ Nanocomposites

The crystalline structures of pure CoAl-LDH, $g\text{-C}_3\text{N}_4$, and a series of $g\text{-C}_3\text{N}_4/\text{CoAl-LDH}$ nanocomposites were characterized by XRD. As Figure 1 shows, two basic diffraction peaks of $g\text{-C}_3\text{N}_4$ located at 13.1° and 27.5° can be indexed to (100) and (002) planes of the $g\text{-C}_3\text{N}_4$ (PDF#50-1250) [32], corresponding to the typical in-planar ordered structure and the interlayer structural stacking of aromatic systems, respectively. The diffractogram of pure CoAl-LDH (PDF# 51-0045) with a typical hydrotalcite-like layer structure exhibits the characteristic diffraction reflections at 11.53° , 23.21° , 34.60° , 38.78° , 45.55° , 60.02° , and 60.90° corresponding to the crystal planes of (003), (006), (012), (015), (018), (110), and (0015), respectively. For the $g\text{-C}_3\text{N}_4/\text{CoAl-LDH}$ nanocomposites, all of the characteristic diffraction peaks of CoAl-LDH can be observed, while it is hard to monitor the typical peaks of $g\text{-C}_3\text{N}_4$ in the $g\text{-C}_3\text{N}_4/\text{CoAl-LDH}_{0.75}$ nanocomposite. However, the characteristic peak intensity of $g\text{-C}_3\text{N}_4$ increases with an increase in the $g\text{-C}_3\text{N}_4$ content of the nanocomposite. It is worth mentioning that the crystal peak (003) which is assigned to CoAl-LDH decreases with the enhanced peak (002) of $g\text{-C}_3\text{N}_4$. Based on (003) and (110) reflections, the lattice parameters of a and c can be calculated. The parameter a is the average distance between two cations in the layers, where $a = 2d_{110}$, and c is three times the distance between the two main body layers, where $c = 3d_{003}$. According to the Debye–Scherrer equation ($D = 0.89\lambda / \beta \cos\theta$, where D is the crystallite size, θ is the Bragg diffraction angle, λ is the radiation wavelength ($\lambda = 1.54$ nm), β represents (003) full width at half maximum), the crystallite size of composites can be obtained [33] and the results are listed in Table 1. As clarified by Table 1, the $g\text{-C}_3\text{N}_4/\text{CoAl-LDH}$ nanocomposites with various $g\text{-C}_3\text{N}_4$ contents give similar values of a and c indicating that the combination of $g\text{-C}_3\text{N}_4$ and LDH does not change the main laminate structure of CoAl-LDH. Among them, the $g\text{-C}_3\text{N}_4/\text{CoAl-LDH}_{1.5}$ nanocomposite displays the narrowest line widths and strongest intense reflections with a stable baseline, indicating the highest crystallinity and the best-crystallized laminated structure.

The morphology and microstructure of $g\text{-C}_3\text{N}_4$, CoAl-LDH, and the $g\text{-C}_3\text{N}_4/\text{CoAl-LDH}$ nanocomposites were explored by SEM. As Figure 2a shows, the $g\text{-C}_3\text{N}_4$ has an irregular two-dimensional (2D) layered structure, and some layers bend to form a tube-like structure with an open end due to its small thickness. Moreover, owing to the large amount of CO_2 and NH_3 produced during the preparation, many pores are formed on the $g\text{-C}_3\text{N}_4$ sheet which, in turn, provide more active sites for the photocatalytic reaction. The CoAl-LDH (Figure 2b) displays irregular lamellae with uniform micron size, but serious layer-by-layer agglomeration is also found with CoAl-LDH sheets, and cannot be effectively dispersed. The $g\text{-C}_3\text{N}_4/\text{CoAl-LDH}$ nanocomposites with various contents of $g\text{-C}_3\text{N}_4$ (Figure 2c–e) display obviously different morphologies as compared with those of the CoAl-LDH and $g\text{-C}_3\text{N}_4$. During the process of coprecipitation, a large amount of metal cations is deposited on the surfaces of $g\text{-C}_3\text{N}_4$, which promotes the intercalation growth of CoAl-LDH nanoflakes on $g\text{-C}_3\text{N}_4$, contributing to mitigation of the self-aggregation of LDH sheets. Upon combination with $g\text{-C}_3\text{N}_4$, CoAl-LDH exhibits a uniform and regular 3D flower-like microsphere structure, which provides a large number of active sites with a larger specific surface area for photocatalytic reactions. In addition, the structure constructed between $g\text{-C}_3\text{N}_4$ and CoAl-LDH provides a suitable electronic heterojunction which can greatly shorten the migration distance of carriers and, thus, promote the photocatalytic reaction. Particularly, more flower-like microspheres with uniform shape and size are formed with the $g\text{-C}_3\text{N}_4/\text{CoAl-LDH}_{1.5}$ nanocomposite as compared with $g\text{-C}_3\text{N}_4/\text{CoAl-LDH}_{0.75}$ and $g\text{-C}_3\text{N}_4/\text{CoAl-LDH}_{1.25}$ nanocomposites, due to the highest crystallinity.

Table 1. The crystallite size and unit cell parameters of the g-C₃N₄/CoAl-LDH nanocomposites.

Sample	Crystallite Size (nm)	a (nm)	c (nm)
g-C ₃ N ₄ /CoAl-LDH _{0.75}	3.034	3.079	22.790
g-C ₃ N ₄ /CoAl-LDH _{1.25}	2.930	3.079	22.906
g-C ₃ N ₄ /CoAl-LDH _{1.5}	2.615	3.076	22.907

**Figure 1.** XRD patterns of CoAl-LDH, g-C₃N₄, and the g-C₃N₄/CoAl-LDH nanocomposites.**Figure 2.** SEM images of: (a) g-C₃N₄; (b) CoAl-LDH; (c) g-C₃N₄/CoAl-LDH_{0.75}; (d) g-C₃N₄/CoAl-LDH_{1.25}; (e) g-C₃N₄/CoAl-LDH_{1.5}; (f) EDS of g-C₃N₄/CoAl-LDH_{1.5}.

The elemental composition of the $g\text{-C}_3\text{N}_4/\text{CoAl-LDH}_{1.5}$ nanocomposite was investigated by EDS spectrum. The results are shown in Figure 2f, where the Au comes from spraying gold in the process of test sample preparation. It was found that the EDS spectra mainly consisted of C, O, N, Al, and Co element, indicating the existence of $g\text{-C}_3\text{N}_4/\text{CoAl-LDH}$. In addition, the relative elemental content of Co to Al in EDS spectrum (5.76 wt% vs. 2.59 wt%) was similar to that of $g\text{-C}_3\text{N}_4/\text{CoAl-LDH}_{1.5}$ (5.21 wt% vs. 2.23 wt%), indicating the consistency of the Co and Al contents in initial precursor and final product.

The N_2 adsorption/desorption isotherms of CoAl-LDH , $g\text{-C}_3\text{N}_4$, and $g\text{-C}_3\text{N}_4/\text{CoAl-LDH}$ nanocomposites were examined to estimate the specific surface area and pore size distribution; the curves are shown in Figure 3. The N_2 adsorption/desorption curves, presented in Figure 3a,b, belong to the typical type IV according to the BDDT classification [34]. The adsorbed quantity increases rapidly in the low-pressure region, followed by a relatively gentle increase trend until the relative pressure (P/P_0) attains 0.8. A drastic increase in adsorption takes place in the high relative pressure level (0.8–1) owing to capillary condensation. A loop appears in the adsorption/desorption curve of the $g\text{-C}_3\text{N}_4/\text{CoAl-LDH}$ nanocomposites at the P/P_0 above 0.5, and there is no obvious saturated adsorption platform, indicating a mesoporous (2–50 nm) structure due to the orderly stacking of the lamellar structure. According to Figure 3c,d, the pore widths of both $g\text{-C}_3\text{N}_4$ and CoAl-LDH are mainly distributed between 2 and 30 nm. After compounding, the pore sizes of the $g\text{-C}_3\text{N}_4/\text{CoAl-LDH}$ nanocomposites are basically maintained.

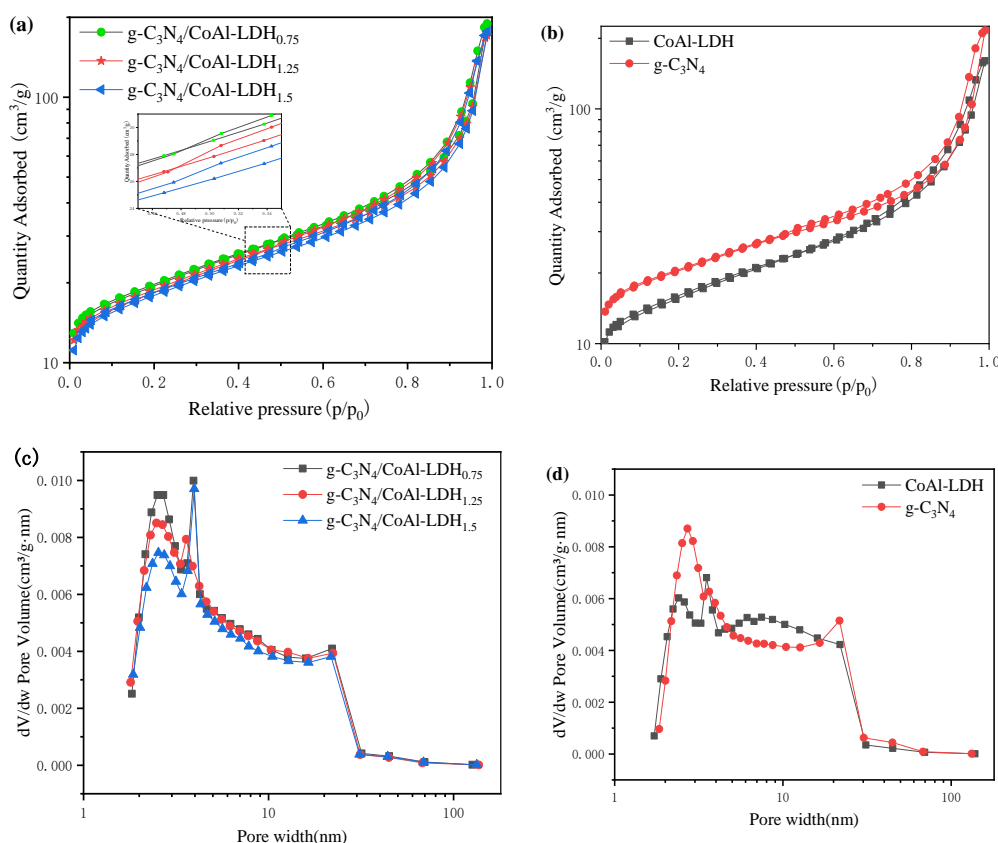


Figure 3. N_2 adsorption/desorption isotherms (a,b) and BJH pore size distribution (c,d) of $g\text{-C}_3\text{N}_4$, CoAl-LDH , and the $g\text{-C}_3\text{N}_4/\text{CoAl-LDH}$ nanocomposites.

The BET surface areas of $g\text{-C}_3\text{N}_4$, CoAl-LDH , and the $g\text{-C}_3\text{N}_4/\text{CoAl-LDH}_{0.75}$, $g\text{-C}_3\text{N}_4/\text{CoAl-LDH}_{1.25}$, and $g\text{-C}_3\text{N}_4/\text{CoAl-LDH}_{1.5}$ nanocomposites are calculated from isotherms to be 71, 57, 66, 63, and 70 m^2/g , respectively. As compared with $g\text{-C}_3\text{N}_4$, the reduction in the pore volume and specific surface area of $g\text{-C}_3\text{N}_4/\text{CoAl-LDH}$ nanocomposites can be ascribed to the blockage of the pores by the incorporation of $g\text{-C}_3\text{N}_4$. Among the

nanocomposites with different $g\text{-C}_3\text{N}_4$ contents, the $g\text{-C}_3\text{N}_4/\text{CoAl-LDH}_{1.5}$ nanocomposite shows the highest pore volume and specific surface area, indicating the incorporation of $g\text{-C}_3\text{N}_4$ nanosheets can effectively improve the dispersion of LDH, which agrees with the result observed from SEM in Figure 2.

The infrared spectra of $g\text{-C}_3\text{N}_4$, CoAl-LDH, and the $g\text{-C}_3\text{N}_4/\text{CoAl-LDH}_{0.75}$, $g\text{-C}_3\text{N}_4/\text{CoAl-LDH}_{1.25}$, and $g\text{-C}_3\text{N}_4/\text{CoAl-LDH}_{1.5}$ nanocomposites are shown in Figure 4. Obviously, the pure $g\text{-C}_3\text{N}_4$ shows an intense band at 808 cm^{-1} , which is attributed to the heptazine ring out-of-plane bending vibration mode. The peaks in the range of $1200\text{--}1650\text{ cm}^{-1}$, such as the characteristic peaks at 1226 , 1311 , 1453 , and 1625 cm^{-1} , are determined to be the stretching vibration of C=N double bond and C-N single bond of aromatic heterocycles. The broad band for N-H stretching vibration is observed from 3000 to 3500 cm^{-1} [35]. For CoAl-LDH, the bands at 750 and 1355 cm^{-1} correspond to the vibration modes of interlayer anion CO_3^{2-} , of which 750 cm^{-1} also refers to the infrared absorption caused by metal-oxygen bond (M-O) [36]. The peak at 3450 cm^{-1} indicates the tensile vibration of the O-H bond in water molecules and the hydrogen bonding of -OH in hydroxides, while the bending vibration of interlayer water molecules causes the characteristic peak at 1629 cm^{-1} .

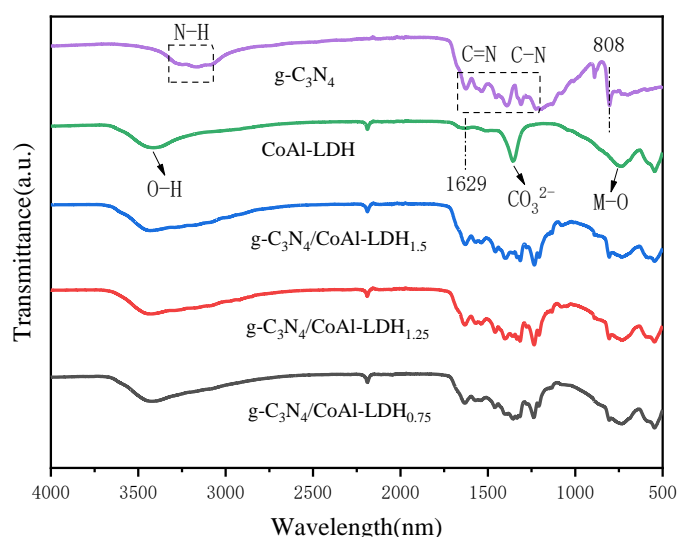


Figure 4. FT-IR spectra of the $g\text{-C}_3\text{N}_4$, CoAl-LDH, and the $g\text{-C}_3\text{N}_4/\text{CoAl-LDH}$ nanocomposites.

The infrared spectrum of the $g\text{-C}_3\text{N}_4/\text{CoAl-LDH}$ nanocomposites basically retain the original vibration modes of $g\text{-C}_3\text{N}_4$ nanosheets and CoAl-LDH. The peaks at 1355 and 1629 cm^{-1} of CoAl-LDH cannot be clearly observed, likely due to overlapping of the characteristic peaks of $g\text{-C}_3\text{N}_4$ in the range of $1200\text{--}1650\text{ cm}^{-1}$. In addition, the absorption peaks of $g\text{-C}_3\text{N}_4$ at 808 cm^{-1} and in the region of $3000\text{--}3500\text{ cm}^{-1}$ show different degrees of red shifting of the $g\text{-C}_3\text{N}_4/\text{CoAl-LDH}$ nanocomposites, resulting in a higher peak wavelength than that of pure $g\text{-C}_3\text{N}_4$. Additionally, the change in the peak positions of the $g\text{-C}_3\text{N}_4/\text{CoAl-LDH}$ nanocomposites indicate that LDH interacts with the N-H group in the $g\text{-C}_3\text{N}_4$ and C-N bonds in the aromatic rings. It should be highlighted that the interface interactions between monomers are beneficial to the transfer of e^- , thus, improving their photocatalytic efficiency. Furthermore, with an increase in $g\text{-C}_3\text{N}_4$ content from 0.75 to 1.5 g/L , an increased peak intensity at 808 cm^{-1} and in the range of $1200\text{--}1650\text{ cm}^{-1}$, bands can be observed, indicating the existence of aromatic rings from $g\text{-C}_3\text{N}_4$ in the $g\text{-C}_3\text{N}_4/\text{CoAl-LDH}$ nanocomposites.

2.2. Optical and Photoelectric Properties of $g\text{-C}_3\text{N}_4$, CoAl-LDH, and the $g\text{-C}_3\text{N}_4/\text{CoAl-LDH}$ Nanocomposites

A UV-VIS spectrophotometer was used to characterize the light-response range and light absorption properties of the $g\text{-C}_3\text{N}_4$, CoAl-LDH, and the $g\text{-C}_3\text{N}_4/\text{CoAl-LDH}$

nanocomposites. As displayed in Figure 5a, the absorption edge of g-C₃N₄ is around 443 nm, reflecting its photocatalytic ability under the UV-visible light irradiation. In addition, three broad absorption peaks located at 460, 490, and 526 nm, the absorption band of CoAl-LDH in the ultraviolet region of 200–300 nm is mainly due to the interlayer ligand-to-metal charge transfer ($O^{2-} \rightarrow Mn^{+}$) [37]. Obviously, owing to the synergistic effect of CoAl-LDH and g-C₃N₄, the g-C₃N₄/CoAl-LDH nanocomposites exhibit typical light absorption bands of CoAl-LDH in the UV-visible light absorption range. The improvement of UV-visible light absorption in the case of g-C₃N₄ is conducive to light utilization rate and generation of photo-induced carriers under illumination, and thus, can strengthen their photocatalytic activity. Moreover, a slight red shift of the absorption edge ranging from 443 to 454 nm is observed for the g-C₃N₄/CoAl-LDH nanocomposites. Among the three nanocomposites with different amounts of g-C₃N₄, the g-C₃N₄/CoAl-LDH_{1.5} nanocomposite shows the best light absorption performance and highest absorption peak intensity. According to the Tauc plot [38], the band gap energies of g-C₃N₄, CoAl-LDH, and the g-C₃N₄/CoAl-LDH_{1.5} nanocomposite were calculated to be 2.66, 2.09, and 2.48 eV, respectively, and are plotted in Figure 5b. Apparently, the embedding of g-C₃N₄ by the CoAl-LDH realizes an intensive UV-visible light absorption due to the change in the band structure and the narrowing of the band gap as compared with pure g-C₃N₄.

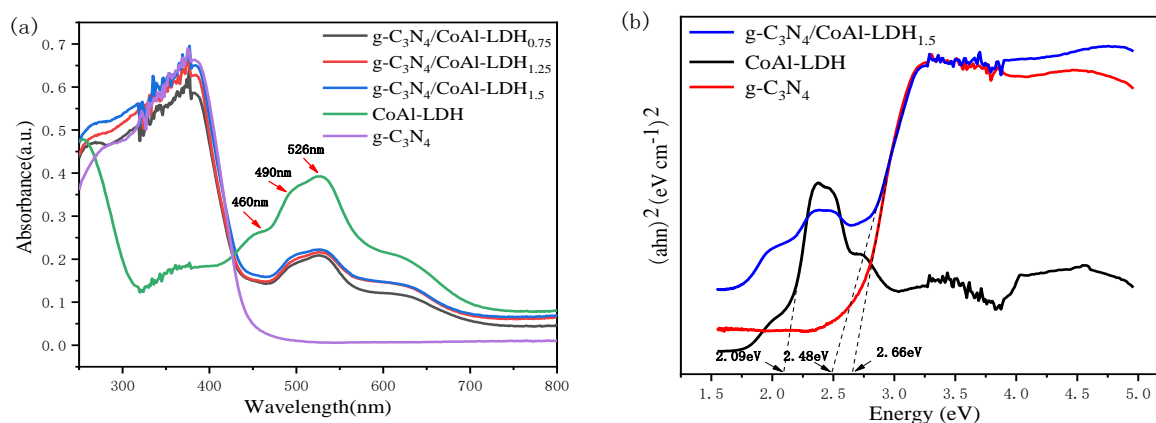


Figure 5. (a) UV-VIS absorption spectra of g-C₃N₄, CoAl-LDH, and the g-C₃N₄/CoAl-LDH nanocomposites; (b) Tauc plot of g-C₃N₄, CoAl-LDH, and the g-C₃N₄/CoAl-LDH_{1.5} nanocomposite.

It is widely acknowledged that the lower PL emission intensity implies a lower rate for charge carrier recombination and higher photocatalytic activity [39]. As depicted in Figure 6, pure g-C₃N₄ displays an intense PL peak at 450 nm indicating a rapid recombination of photo-excited carriers, which is in accordance with the results presented in Figure 5a. In contrast to g-C₃N₄, the PL emission intensities of the g-C₃N₄/CoAl-LDH nanocomposites are decreased obviously and show a blue shift. This suggests that CoAl-LDH can accelerate electron–hole separation and the transfer process owing to the formation of heterojunction with g-C₃N₄, and therefore, impedes the electron–hole recombination. The smallest PL emission intensity is found for the g-C₃N₄/CoAl-LDH_{1.5} nano composite, which indicates that higher recombination of carriers can be hindered with a higher content of g-C₃N₄. This could ascribe to the fact that the g-C₃N₄/CoAl-LDH_{1.5} nanocomposite has the highest crystallinity and can provide an efficient transfer of excited carriers between the interfaces of LDH and g-C₃N₄.

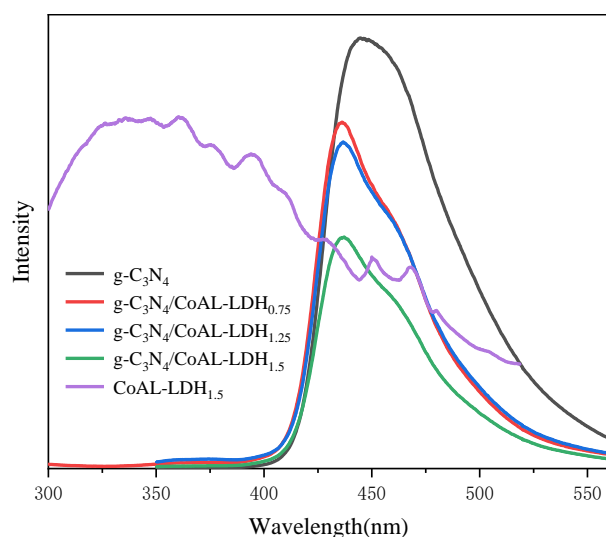


Figure 6. PL spectra of the $g\text{-C}_3\text{N}_4$, CoAl-LDH, and the $g\text{-C}_3\text{N}_4/\text{CoAl-LDH}$ nanocomposites.

To further explore the electron–hole separation and transfer behavior of the $g\text{-C}_3\text{N}_4/\text{CoAl-LDH}_{1.5}$ nanocomposite, EIS and photocurrent transient were performed, and the obtained plots are exhibited in Figure 7. Figure 7a gives the EIS Nyquist plots of $g\text{-C}_3\text{N}_4$, CoAl-LDH and the $g\text{-C}_3\text{N}_4/\text{CoAl-LDH}_{1.5}$ nanocomposite. Note that the radius of circular arc in Nyquist plot reflects the resistance of carrier immigration on the surface of photocatalytic materials [40]. The small arc radius at high frequency suggests a more effective separation and a faster interfacial transfer of excited carrier [41]. Among all the samples, the $g\text{-C}_3\text{N}_4/\text{CoAl-LDH}_{1.5}$ nanocomposite displays the smallest arc radius, suggesting the lowest resistance to electron transfer. This demonstrates that the heterojunction constructed between $g\text{-C}_3\text{N}_4$ and LDH indeed has a positive effect on the efficiency of excited carrier separation and transfer.

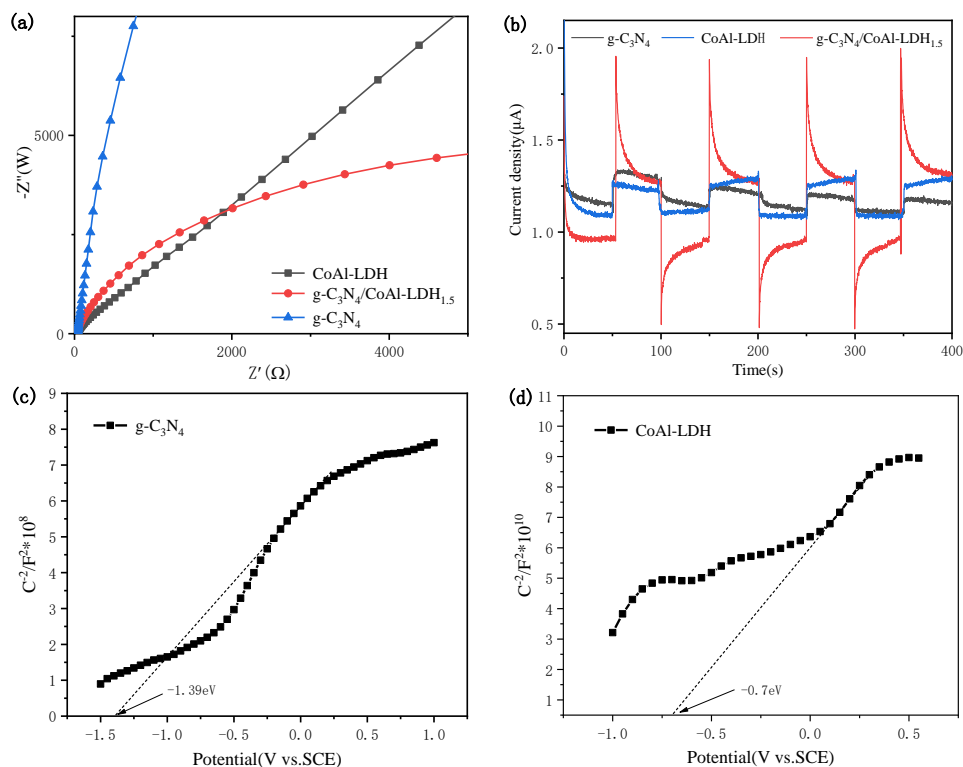


Figure 7. (a) EIS Nyquist plots; (b) I-T plots of $g\text{-C}_3\text{N}_4$, CoAl-LDH, and the $g\text{-C}_3\text{N}_4/\text{CoAl-LDH}_{1.5}$ nanocomposite. Mott–Schottky plots of: (c) $g\text{-C}_3\text{N}_4$; (d) CoAl-LDH.

The photocurrent transient response of $g\text{-C}_3\text{N}_4$, CoAl-LDH and the $g\text{-C}_3\text{N}_4/\text{CoAl-LDH}_{1.5}$ nanocomposite film electrodes were investigated through four light-dark cycles, and the I-T plots are shown in Figure 7b. Due to the narrow band gap (2.09 eV), CoAl-LDH can only produce weak photocurrent with irradiation, indicating that the photo-generated carriers have a short lifetime, and can recombine easily in the bulk phase of the material. In contrast to the pure LDH and $g\text{-C}_3\text{N}_4$, the $g\text{-C}_3\text{N}_4/\text{CoAl-LDH}_{1.5}$ nanocomposite shows a higher photocurrent intensity, which indicates that the heterojunction structure constructed can accelerate the transfer of photo-induced electrons and prolong their lifetimes, and consequently inhibit the recombination of photo-induced carriers. It can be extracted that the light current intensity of the $g\text{-C}_3\text{N}_4/\text{CoAl-LDH}_{1.5}$ nanocomposite is the highest, which is about 2.4 and 3.2 times that of CoAl-LDH and $g\text{-C}_3\text{N}_4$, respectively.

The M-S measurement was investigated to examine the electronic potentials of $g\text{-C}_3\text{N}_4$ and CoAl-LDH. The obtained M-S plots are displayed in Figure 7c,d. By extending the linear plots to the X axis, corresponding to $Y = 0$, the positive slopes in M-S plots indicates n-type semiconductor characteristics for both $g\text{-C}_3\text{N}_4$ and CoAl-LDH [42]. The flat band potentials (vs. SCE) of $g\text{-C}_3\text{N}_4$ and CoAl-LDH are -1.39 and -0.7 eV, respectively, which is approximately equal to their conduction band (CB) potential. Furthermore, according to the formula $E_g = E_{VB} - E_{CB}$, the valence band (VB) values (vs. SCE) of $g\text{-C}_3\text{N}_4$ and CoAl-LDH are calculated as 1.27 and 1.39 eV, respectively. Therefore, it can be expected that the staggered energy band structure of $g\text{-C}_3\text{N}_4$ and CoAl-LDH can form a type II heterojunction electric field at the interface between $g\text{-C}_3\text{N}_4$ and CoAl-LDH, which greatly improves the separation and transfer of photo-induced electron-hole pairs.

2.3. Photocatalytic Depollution Activity of $g\text{-C}_3\text{N}_4$, CoAl-LDH and the $g\text{-C}_3\text{N}_4/\text{CoAl-LDH}$ Nanocomposites

The photocatalytic activities of $g\text{-C}_3\text{N}_4$, CoAl-LDH and the $g\text{-C}_3\text{N}_4/\text{CoAl-LDH}$ nanocomposites were investigated in view of NO_x degradation. As shown in Figure 8, after irradiation with UV-visible light for 30 min, the degradation efficiencies of NO_x by $g\text{-C}_3\text{N}_4$ and LDH were 72.87% and 27.92%, respectively. For the $g\text{-C}_3\text{N}_4/\text{CoAl-LDH}$ nanocomposites, the photocatalytic depollution efficiency of NO_x gradually improved with an increase in $g\text{-C}_3\text{N}_4$ content, which was in accordance with the results from other measurements, such as PL, EIS, UV-VIS, and I-T. In particular, the $g\text{-C}_3\text{N}_4/\text{CoAl-LDH}_{1.5}$ nanocomposite had the highest NO_x degradation efficiency (89.62%), which was around 1.23 and 3.21 times that of $g\text{-C}_3\text{N}_4$ and LDH, respectively. The higher NO_x degradation efficiency achieved by the $g\text{-C}_3\text{N}_4/\text{CoAl-LDH}$ nanocomposites can be ascribed to the formation of a type II heterojunction between $g\text{-C}_3\text{N}_4$ and CoAl-LDH. In addition, the NO_x degradation performance of the $g\text{-C}_3\text{N}_4/\text{CoAl-LDH}_{1.5}$ nanocomposite was compared with other $g\text{-C}_3\text{N}_4$ -based photocatalytic materials (Table 2). As can be seen from Table 2, the NO_x degradation rate of the $g\text{-C}_3\text{N}_4/\text{CoAl-LDH}_{1.5}$ nanocomposite is outstanding as compared with other $g\text{-C}_3\text{N}_4$ -based materials.

Table 2. Comparison of NO_x degradation performances of selected $g\text{-C}_3\text{N}_4$ -based photocatalysts.

Photocatalyst	NO (ppm)	Amount (mg)	Degradation Rate η (%)	Incident Light (nm)	References
$g\text{-C}_3\text{N}_4/\text{CoAl-LDH}_{1.5}$	0.5	25	89.62	320~780 nm	This work
$g\text{-C}_3\text{N}_4/\text{SnO}_2$	0.5	200	44.17	>325 nm	[43]
$\text{Bi}_2\text{O}_3/g\text{-C}_3\text{N}_4$	0.5	200	39.1	\	[44]
$\text{W}_{18}\text{O}_{49}/g\text{-C}_3\text{N}_{4-x}$	0.6	50	83.55	Simulated sunlight	[45]
GNC-0.3	1.339	300	59.1	>400 nm	[46]
(Na-Ca co-doped $g\text{-C}_3\text{N}_4$)	0.6	50	80	>420 nm	[47]
p-type $g\text{-C}_3\text{N}_4$	0.6	50	65	Visible light	[48]
$g\text{-C}_3\text{N}_4$ QDs/ InVO_4	0.4	50	68	Visible light	[49]
$\text{Sb}_2\text{WO}_6/g\text{-C}_3\text{N}_4$	0.6	20	60	>420 nm	[50]

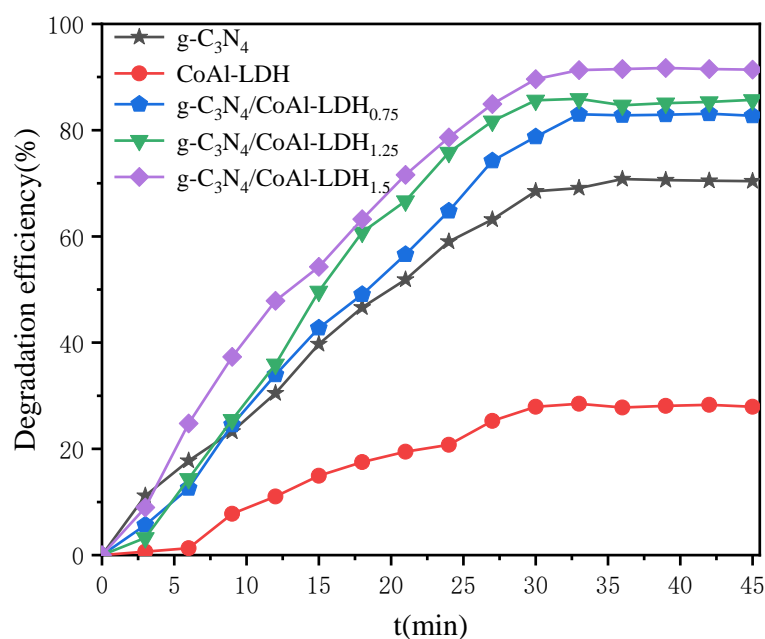


Figure 8. Photocatalytic degradation of NO_x by g-C₃N₄, CoAl-LDH, and the g-C₃N₄/CoAl-LDH nanocomposites.

2.4. Photocatalytic Activity of the g-C₃N₄/CoAl-LDH Nanocomposites in Cement Mortars

2.4.1. Effect of High Alkalinity of the Cementitious Materials on Photocatalytic Ability

The compatibility between cement and a photocatalytic material should be considered when a photocatalyst is mixed with cement. In the process of cement hydration, plenty of calcium hydroxide is commonly produced resulting in an alkaline environment. Such a high alkalinity could be harmful to the photocatalytic capacity of some photocatalysts, for instance, affecting energy band structure, increasing electron–hole pair recombination efficiency, and decreasing service life [51]. Therefore, it is necessary to protect a photocatalyst from the cement matrix. In order to evaluate the alkaline impact on photocatalytic capacity, the powders of g-C₃N₄ and the g-C₃N₄/CoAl-LDH_{1.5} nanocomposite were immersed in simulated concrete pore solution for 10 min, and thereafter, washed and dried at 60 °C. Figure 9 shows the PL spectra of g-C₃N₄ and the g-C₃N₄/CoAl-LDH_{1.5} nanocomposite before and after immersing treatment by simulated concrete pore solution (0.6 mol/L KOH, 0.2 mol/L NaOH, 0.001 mol/L Ca(OH)₂, and 0.8 mol/L NaHCO₃). According to Figure 9, the PL intensity becomes stronger after the treatment for both g-C₃N₄ and the g-C₃N₄/CoAl-LDH_{1.5} nanocomposite, suggesting that the two treated photocatalysts have a higher recombination probability of photo-induced carriers. This pH-dependent PL behavior can be attributed to the existence of free zigzag sites, as previously reported graphene quantum dots (GOD) for a similar structure between graphene and g-C₃N₄ [52]. However, it is worth mentioning that the alkaline effect on the g-C₃N₄/CoAl-LDH_{1.5} nanocomposite is smaller than that on g-C₃N₄, since only a slight increase in PL intensity could be observed with the g-C₃N₄/CoAl-LDH_{1.5} nanocomposite after the alkaline treatment. As mentioned above, the molecular structure of LDH shares the same molecular characteristics with some cement hydration products and, thus, exhibits good compatibility with cement-based materials as well as chemical stability in an alkaline environment [23–25]. From this point of view, the incorporation of g-C₃N₄ into CoAl-LDH has indeed effectively mitigated the possible adverse effect of high alkalinity of a cement-based system on the photocatalytic capacity.

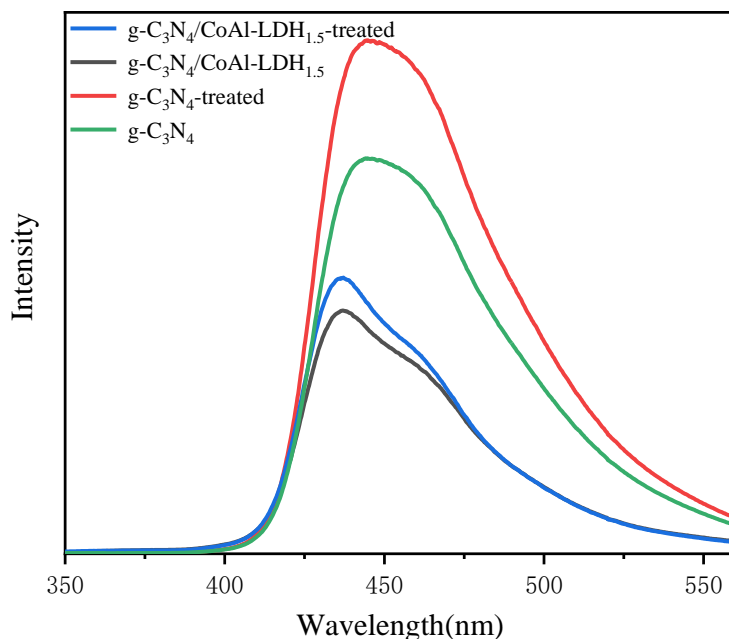


Figure 9. PL spectra of $g\text{-C}_3\text{N}_4$ and the $g\text{-C}_3\text{N}_4/\text{CoAl-LDH}_{1.5}$ nanocomposite before and after immersing treatment by simulated concrete pore solution.

2.4.2. Photocatalytic Performance Investigation in Cement Mortars

NO_x degradation of the M, MC, ML, MM, and CNMM mortar samples was examined to evaluate their photocatalytic performance and the results are shown in Figure 10. Obviously, the degradation efficiency of the MM sample is greater than that of the CNMM sample under the UV-visible light irradiation. This implies that CoAl-LDH can protect $g\text{-C}_3\text{N}_4$ from the alkaline effect of cementitious materials. Hence, it can be concluded that the presence of CoAl-LDH can prevent the destruction of $g\text{-C}_3\text{N}_4$ in alkaline cement mortar, and also significantly improve the photocatalytic capacity by its synergistic effect.

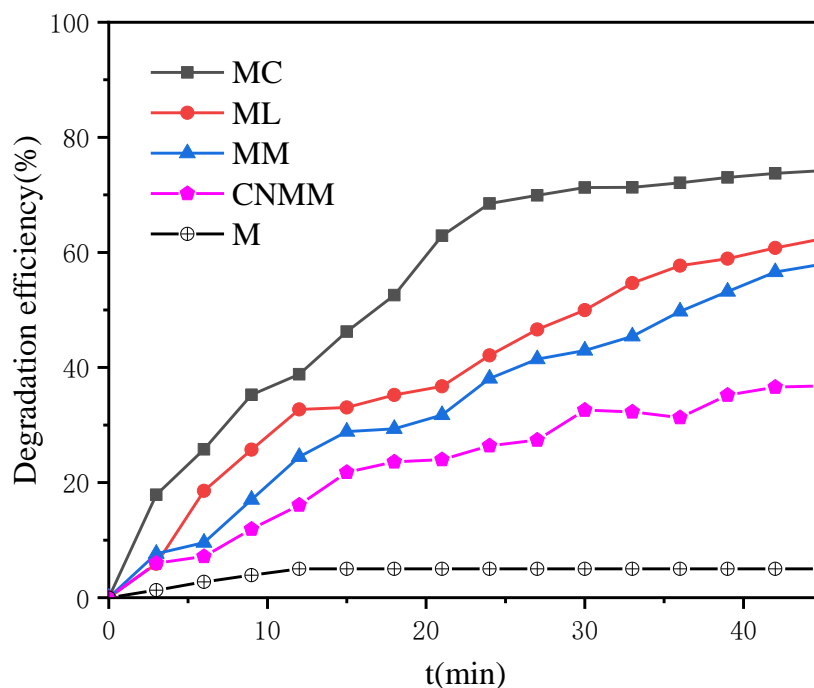


Figure 10. Photocatalytic NO_x degradation efficiency of different cement mortars.

To further analyze the influence of different manufacturing methods on photocatalytic degradation, a specified test was carried out on various types of mortars. For the reference mortar, a certain degradation rate (5%) is observed in the first 30 min, which is mainly due to its absorption. In contrast, the mortar coated with the $g\text{-C}_3\text{N}_4/\text{CoAl-LDH}_{1.5}$ nanocomposite (MC sample) shows the highest photocatalytic performance with a degradation efficiency up to 71.29% after 30 min of UV-visible light irradiation. After that, the degradation efficiency reaches a steady-state platform of 74.21% at 45 min. As compared with the first 20 min, the slowing down of the photocatalytic degradation rate of the MC sample can be ascribed to the shielding effect of reaction products on the active site of photocatalyst. Among all the mortars, the ML and MM samples exhibit a middle-level photocatalytic performance with degradation efficiencies up to 61.4% and 58.97%, respectively, after 45 min irradiation, but no steady-state plateau is observed. In summary, all the mortar samples fabricated by internal mixing, coating, and spraying can effectively degrade the NO_x pollutant in a relatively short period under UV-visible light.

2.4.3. Effect of Wearing on NO_x Degradation Efficiency

The NO_x degradation efficiencies for both the original and wearing samples after the rotary abrasion process are shown in Figure 11. It can be seen that the degradation efficiencies of the ML and MC mortar samples are decreased to a certain extent after the wearing operation. In particular, the photocatalytic degradation efficiency of the MC sample decreases by 17.21% after wearing for 10 min. As for the ML sample, the wearing action causes a significant reduction in the photocatalytic degradation efficiency, dropping from 62.4% to 33.8%. For the control sample (M), wearing has little influence of wearing on its removal rate of NO_x . Nevertheless, the photocatalytic efficiencies of the MM and CNMM samples were slightly higher than those before wearing, which can be ascribed to the exposure of photocatalysts on the specimen surface under abrasion. In general, the photocatalytic degradation efficiency of mortar incorporated with the $g\text{-C}_3\text{N}_4/\text{CoAl-LDH}_{1.5}$ nanocomposite presents abrasive resistance, although it is decreased after wearing.

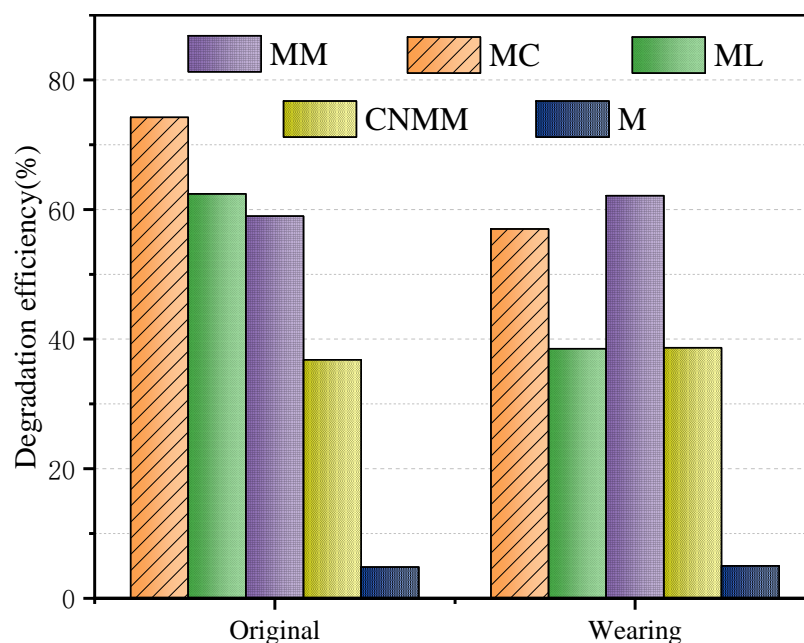


Figure 11. Photocatalytic NO_x degradation efficiency of different cement mortars after wearing.

The microstructure and morphology of the coated mortars before and after the wearing tests were investigated by SEM-EDS. As shown in Figure 12, thin layers of $g\text{-C}_3\text{N}_4/\text{CoAl-LDH}$ -based coatings can be observed, and are loading uniformly on the raw surface of the mortars' substrates. Obviously, the porous microstructures of both the MC (Figure 12a) and

ML (Figure 12b) mortar substrates provide good anchorages for the photocatalytic coatings. In addition, a lot of particulate matter was found distributed on the surface of the ML sample (Figure 12d) without adequate adhesion. For the MC sample (Figure 12c), due to the adhesion of cement binder, a smooth surface with a photocatalytic coating is observed without obvious particles and cracks. Figure 12e,f show the surface morphologies of the MC and ML samples, respectively, after the rotary abrasion process. For the MC sample, the wearing action results in a partial exfoliation of the g-C₃N₄/CoAl-LDH_{1.5}-based coating and a relatively rough surface. In case of the ML sample, a rougher surface morphology is observed after the wearing, due to the loss of paste layer from the mortar substrate.

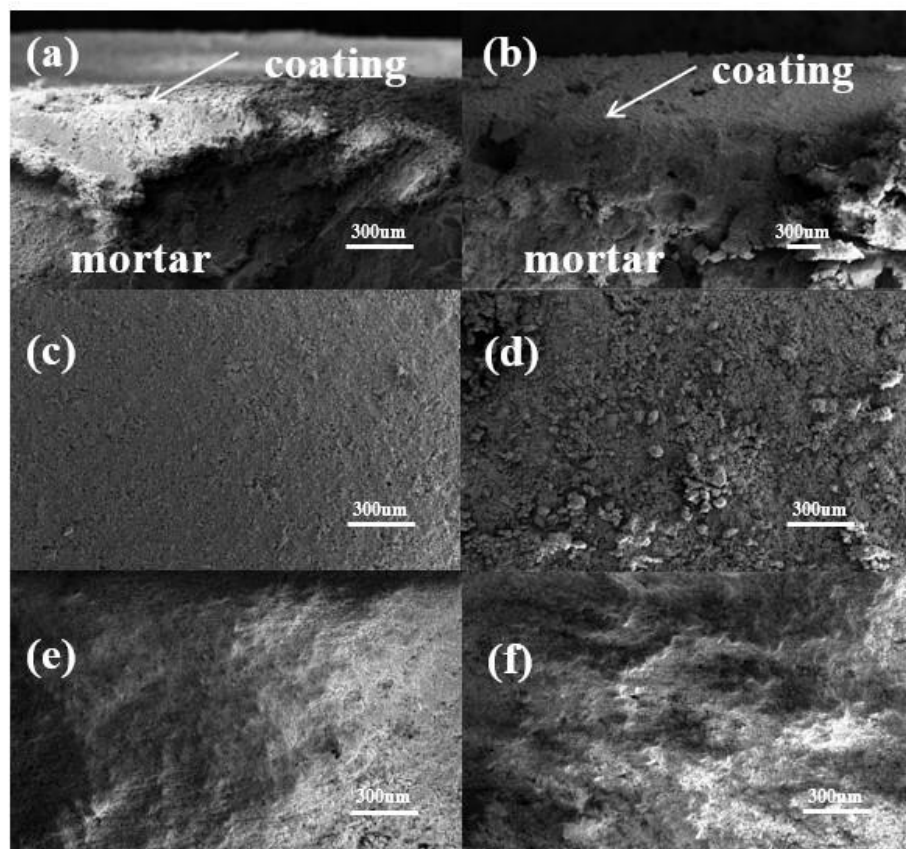


Figure 12. Morphologies of the cross sections and surfaces of the coated mortars before and after wearing: (a,c,e) for MC; (b,d,f) for ML.

Figure 13 shows the EDS spectra of the coated mortars before and after wearing. Except for the Au coming from spraying gold in the process of test sample preparation, the Co signal is regarded as coming from the g-C₃N₄/CoAl-LDH_{1.5} nanocomposite which is attached on the surface of the coated mortars. The concentration of Co on the mortar surface after the wearing process is obviously declined. Particularly, the MC sample shows a reduction in Co content from 11.77% to 6.77% because of the wearing. As compared with the MC sample, the ML sample exhibits a lower decrease in Co content after wearing. The results of the SEM-EDS reveal that both of the MC and ML samples display a certain resistance to abrasive action, a finding similar to the results of NO_x degradation tests.

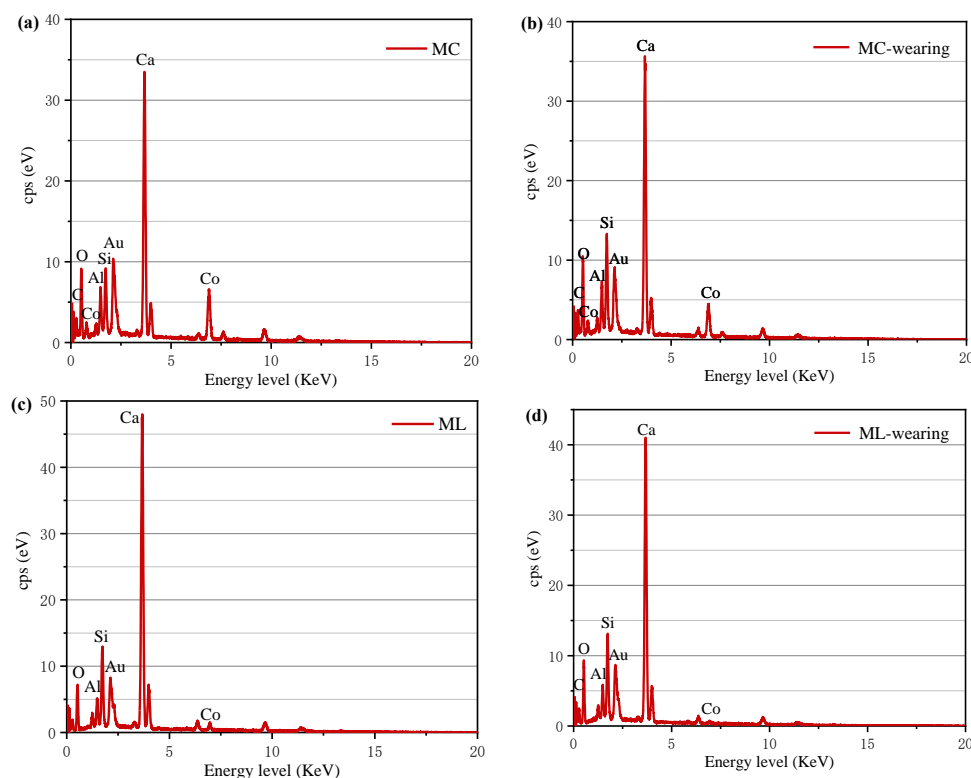


Figure 13. EDS spectra for the coated mortars before and after wearing: (a,b) MC; (c,d) ML.

3. Experimental

3.1. Materials

Ammonium fluoride (NH_4F), urea ($\text{CO}(\text{NH}_2)_2$), aluminum nitrate nonahydrate ($\text{Al}(\text{NO}_3)_3 \cdot 9\text{H}_2\text{O}$), citric acid monohydrate ($\text{C}_6\text{H}_{10}\text{O}_8$), and cobalt nitrate hexahydrate ($\text{Co}(\text{NO}_3)_2 \cdot 6\text{H}_2\text{O}$) were purchased from National Medicine Group Chemical Reagent Co., Ltd., Shanghai, China. The Portland cement (42.5R-grade) was produced from the Fujian Cement Co., Ltd, Fuzhou, China was used.

3.2. Preparation of $g\text{-C}_3\text{N}_4/\text{CoAl-LDH}$

Synthesis of $g\text{-C}_3\text{N}_4$: As described in a previous study [35], $g\text{-C}_3\text{N}_4$ was prepared by condensation polymerization of urea under environmental pressure and self-supporting atmosphere produced by pyrolysis. Briefly, 20 g urea and 25 mg citric acid monohydrate were mixed first, before being put into a covered crucible and calcined at 550°C for 240 min. After cooling naturally, the powders of $g\text{-C}_3\text{N}_4$ were obtained by milling the light-yellow agglomerates.

Synthesis of $g\text{-C}_3\text{N}_4/\text{CoAl-LDH}$: The $g\text{-C}_3\text{N}_4/\text{CoAl-LDH}$ was synthesized through a coprecipitation process [53]. Firstly, a 100 mL mixed solution containing $\text{Al}(\text{NO}_3)_3 \cdot 9\text{H}_2\text{O}$ (0.0075 mol), urea (0.27 mol), $\text{Co}(\text{NO}_3)_2 \cdot 6\text{H}_2\text{O}$ (0.0225 mol), and NH_4F (1 g/L) was prepared in a beaker before adding a given content of $g\text{-C}_3\text{N}_4$. Then, the mixture was stirred rapidly for 60 min at 25°C , and continuously, for another 24 h at 110°C . Finally, the precipitate was washed, and dried in an oven for a day at 60°C . The resulting products prepared by adding 0.75, 1.25, and 1.5 g/L $g\text{-C}_3\text{N}_4$ were named as $g\text{-C}_3\text{N}_4/\text{CoAl-LDH}_{0.75}$, $g\text{-C}_3\text{N}_4/\text{CoAl-LDH}_{1.25}$, and $g\text{-C}_3\text{N}_4/\text{CoAl-LDH}_{1.5}$, respectively. For comparison, pure CoAl-LDH was also prepared following the same procedure except for the omission of $g\text{-C}_3\text{N}_4$. The synthesis ratio of the above photocatalyst materials is listed in Table 3.

Table 3. Proportion of the CoAl-LDH and the g-C₃N₄/CoAl-LDH nanocomposites.

Sample	g-C ₃ N ₄ (g/L)	Al(NO ₃) ₃ ·9H ₂ O (mol)	Co(NO ₃) ₂ ·6H ₂ O (mol)	Urea (mol)	NH ₄ F (g/L)
CoAl-LDH	0	0.0075	0.0225	0.27	1
g-C ₃ N ₄ /CoAl-LDH _{0.75}	0.75	0.0075	0.0225	0.27	1
g-C ₃ N ₄ /CoAl-LDH _{1.25}	1.25	0.0075	0.0225	0.27	1
g-C ₃ N ₄ /CoAl-LDH _{1.5}	1.5	0.0075	0.0225	0.27	1

3.3. Preparation of Photocatalytic Cement Mortars

Five groups of mortar specimens were fabricated: reference cement mortar (M), cement mortar with a thin layer of cement paste containing g-C₃N₄/CoAl-LDH (ML), cement mortar with g-C₃N₄/CoAl-LDH coating (MC), cement mortar admixed with g-C₃N₄/CoAl-LDH (MM), and cement mortar admixed g-C₃N₄ (CNMM). The cement mortar samples were prepared with the water/cement/standard sand at the mass ratio of 0.5:1:3, according to the standard procedure (UNI 11259:2008 standard [54]). The fresh mortars were cast into the cubic mold (40 × 40 × 40 mm³), demolded after one day, and then, cut into two halves, donated as the M sample. For the preparation of the MM sample, g-C₃N₄/CoAl-LDH powder (0.25% by the weight of cement) was ultrasonically dispersed in water for 10 min before adding into the dry mixture of cement mortar. Then, the mixture was stirred evenly and cast into molds. For the preparation of the CNMM sample, the same procedure was applied but g-C₃N₄/CoAl-LDH was replaced with g-C₃N₄. To obtain the ML sample, first, fresh cement paste mixed with 0.25 wt% g-C₃N₄/CoAl-LDH with a water-to-cement ratio of 0.5 was prepared, and then spread on the cut face of the prepared mortar with a thickness of around 5 mm. To obtain the MC sample, the g-C₃N₄/CoAl-LDH suspension (10 g/L) with cement as binder (10% by the weight of water) was deposited on the fresh mortar by spraying. The parameters for the spraying operation were as following: spraying pressure is 7.0 MPa; diameter of nozzle is 1.3 mm; distance between the spray device and specimen is 25 cm; spraying angle is 45°, and spray time lasts for 1 min. The samples were all cured in a standard curing room (25 °C and 98% RH) for 28 days. The mix designs of the photocatalytic cement mortars are listed in Table 4. The images of photocatalytic cement mortars MC, ML, MM, and CNMM are presented in Figure 14.

Table 4. Mix designs of the photocatalytic cement mortars.

Sample	Cement (g)	Sand (g)	g-C ₃ N ₄ /CoAl-LDH (g)	g-C ₃ N ₄ (g)	w/c
MC	152	450	0.2		0.5
ML	170	450	0.05		0.5
MM	150	450	0.37		0.5
CNMM	150	450		0.37	0.5

**Figure 14.** Photocatalytic cement mortars (a) MC; (b) ML; (c) MM; (d) CNMM.

3.4. Characterization and Measurement

The X-ray diffraction (XRD) analysis was performed on a DY5261/Xpert3 with Cu K α irradiation ($\lambda = 0.154$ nm, 45 kV, and 40 mA) at a scanning rate of 10°/min. The morphologies and elemental analysis of the samples were performed on a scanning electron

microscopy (TECNAI G2 F20) combined with an energy-dispersive X-ray spectroscopy (SEM-EDS). The specific area and pore size distribution were determined using a surface area and porosity analyzer (ASAP 2460, Micromeritics Instruments Inc., Norcross, Georgia, USA). Before the specified test, samples were degassed and dried for 12 hrs. The Fourier transform infrared spectra (FTIR) of the samples were recorded using a FTIR spectrometer (AVATAR360) in the scanning range of 4000–400 cm^{-1} . The optical absorbance was measured by UV-VIS spectrophotometry with a Cary 7000 UV-VIS spectrometer from 200 to 800 nm using barium sulfate as background. Steady-state photoluminescence spectra were tracked using a Fluorescence Spectrometer (F-7000, Hitachi, Japan). The excitation wavelength of g-C₃N₄ and g-C₃N₄/CoAl-LDH is 285 nm, and that of CoAl-LDH is 255 nm.

The photoelectric tests were performed using a CHI760 electrochemical workstation. The electrochemical cell was set up with a platinum electrode, a saturated calomel electrode (SCE), and a working electrode using 0.1 mol/L sodium sulfate solution as the electrolyte. In this work, the photocatalytic film electrode, as the working electrode, was obtained by depositing the photocatalyst suspension on fluorine-doped tin oxide conductive glass. The electrochemical impedance spectroscopy (EIS) was measured under open circuit potential condition. The Mott–Schottky (M-S) plots were measured at 800 Hz and 1200 Hz, respectively. The photocurrent test was conducted with an initial voltage of 0.4 V in the two-electrode system.

3.5. Photocatalytic Measurement

The photocatalytic oxidation of nitric oxide (NO_x) was carried out using a customized reaction setup as depicted in Figure 15. It consists of a gas supply providing 5 ppmv (parts per million by volume) NO stabilized in nitrogen (N₂) and synthetic air, a xenon lamp, a reactor cell housing the test samples, and a NO_x analyzer. The xenon lamp of 300 W worked as the light source ($\lambda = 320\sim 780$ nm), and the irradiance could be adjusted via the distance between the lamp and sample. The data acquisition of NO_x concentration was performed using a NO_x analyzer (Gastiger 6000) in a time interval of 5 s. All the photocatalytic experiments were conducted under stable conditions as listed in Table 5.

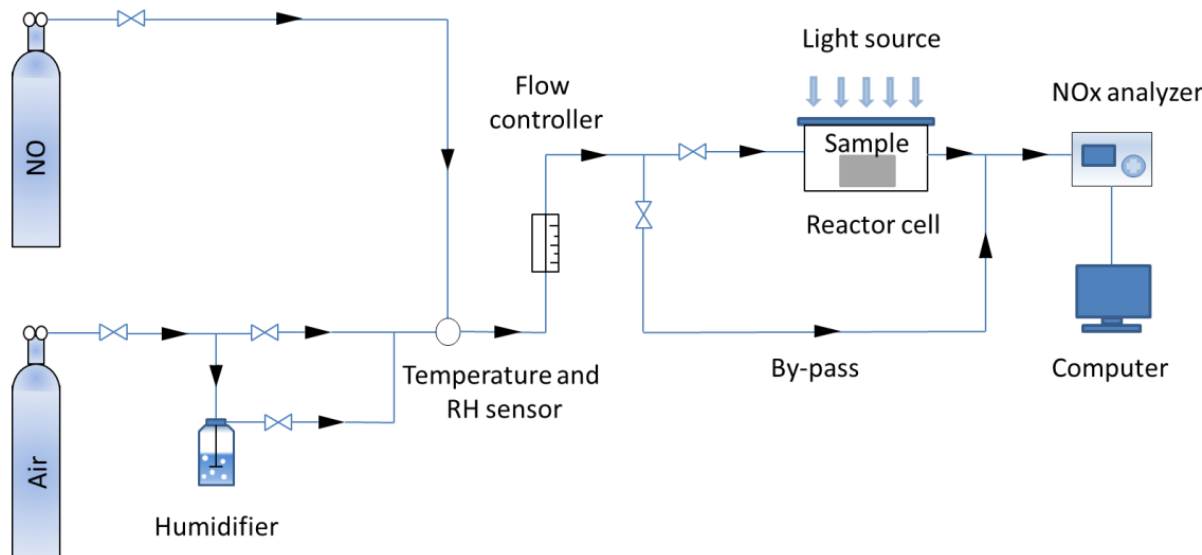


Figure 15. Schematic diagram of the NO_x degradation reaction device.

Table 5. Photocatalytic experimental conditions.

Parameter	Value
Temperature (°C)	25
Relative humidity (%)	50
Initial NO concentration (ppmv)	0.5
Flow rate of gas mixtures (L/min)	3
Light intensity on the sample surface (mW/cm ²)	85

To evaluate the photocatalytic depollution activity, 25 mg photocatalyst powders were suspended in 5 mL deionized water, poured into a glass dish ($\Phi = 5$ cm), and then dried in an oven at 60 °C. Before irradiation, the prepared photocatalyst sample was put into the reactor cell, and let the gas mixture flow through for a certain time to achieve an initial stable condition. Once a stable NO concentration was reached, the valve was turned off, allowing the absorption of NO on the sample in a dark state until saturation. Then, the sample was exposed to the UV-visible light through quartz glass for 45 min of degradation reaction. The concentration of the NO_x was continually monitored until switching off the xenon lamp for a few minutes. To evaluate the performance of photocatalytic mortar, the same procedure was applied by using four series of mortar samples as fabricated in Section 2.3.

The photocatalytic activity of each testing sample is characterized by the NO_x conversion efficiency and calculated as follows [55]:

$$\eta = \frac{[C_{\text{NO}_x}]_{\text{in}} - [C_{\text{NO}_x}]_{\text{out}}}{[C_{\text{NO}_x}]_{\text{in}}} \times 100\% \quad (1)$$

where $[C_{\text{NO}_x}]_{\text{in}}$ is the initial concentration of NO_x (ppm) before irradiation and $[C_{\text{NO}_x}]_{\text{out}}$ is the outlet concentration of NO_x (ppm) after switching off the light.

3.6. Laboratory-Simulated Wearing and Abrasion

The abrasion and wear resistance of mortars coated with photocatalyst (ML and MC) were evaluated through a rotary abrasion process. An electric grinding rod was utilized to simulate a scaled wheel passing back and forth on the specimen in wearing condition. The grinding rod was applied for 10 min at a speed of 150 rpm/min under constant loading of 75 N. The photocatalytic behaviors along with the surface morphologies of the mortar samples were examined by SEM-EDS through comparative observations and quantitative analyses of Co element in the samples before and after the wearing.

4. Conclusions

Novel organic-inorganic g-C₃N₄/CoAl-LDH nanocomposites were synthesized in this work. The g-C₃N₄/CoAl-LDH nanocomposites were characterized comprehensively by means of XRD, SEM, BET, FTIR, PL, and photoelectric tests. A series of g-C₃N₄/CoAl-LDH photocatalytic cement mortars were prepared. The photocatalytic activities of g-C₃N₄, CoAl-LDH, and the g-C₃N₄/CoAl-LDH nanocomposites and the corresponding mortars were evaluated based on NO_x degradation under UV-visible light. The main conclusions are summarized as follows:

- (1) A group of g-C₃N₄/CoAl-LDH nanocomposites with unique flower-like microsphere structures were synthesized through coprecipitation method. The microstructures of the g-C₃N₄/CoAl-LDH nanocomposites were affected by g-C₃N₄ content.
- (2) Formation of the heterojunction in the g-C₃N₄/CoAl-LDH nanocomposites was demonstrated. The g-C₃N₄/CoAl-LDH nanocomposites exhibited overall better photocatalytic performances than pure g-C₃N₄ and CoAl-LDH. A higher content of g-C₃N₄ leads to an increase in crystallinity, specific surface area, light response range, and electron-hole separation rate. The photocatalytic capacity of the g-C₃N₄/CoAl-LDH nanocomposites is enhanced accordingly.

- (3) A higher photocatalytic capacity was found in the g-C₃N₄/CoAl-LDH cement mortar than in the g-C₃N₄ cement mortar in view of NO_x degradation. A sufficient combination of g-C₃N₄ with LDH can effectively accelerate the separation and transfer of photo-induced carriers, and also prevent the reduction in photocatalytic ability caused by the high alkalinity of cementitious materials.
- (4) The g-C₃N₄/CoAl-LDH photocatalytic cement mortars, including those fabricated by internal mixing, coating, and spraying, can effectively degrade NO_x pollutant in a relatively short period under UV-visible light, and they all present good wear.

Author Contributions: Conceptualization, Z.Y.; Data curation, M.H., L.L., J.X. and W.W.; Formal analysis, M.H., L.L., J.X., and W.W.; Investigation, L.L. and W.W.; Methodology, M.H. and J.X.; Project administration, Z.Y.; Supervision, Z.Y. and C.Y.; Validation, L.L. and W.W.; Writing—original draft, M.H. and J.X.; Writing—review and editing, Z.Y. and C.Y. All authors have read and agreed to the published version of the manuscript.

Funding: This research was funded by the Natural Science Foundation of Fujian Province (2019J01235), the Natural Science Foundation of China (51978171, U1905214), the Fuzhou Science and Technology Bureau (2021-P-031), National Key Technologies R&D Program of China (2018YFA0209301) and the Minjiang Scholar program of Fujian province, China (GXRC-19045).

Data Availability Statement: The data presented in this study are available on request from the corresponding author.

Conflicts of Interest: The authors declare no conflict of interest.

References

1. Lasek, J.; Yu, Y.H.; Wu, J.C. Removal of NO_x by photocatalytic processes. *Photochem. Photobiol.* **2013**, *14*, 29–52. [[CrossRef](#)]
2. Yang, L.; Hakki, A.; Wang, F.; Macphee, D.E. Different roles of water in photocatalytic DeNO_x mechanisms on TiO₂: Basis for engineering nitrate selectivity? *Appl. Mater. Interfaces* **2017**, *9*, 17034–17041. [[CrossRef](#)] [[PubMed](#)]
3. Sugrañez, R.; Álvarez, J.I.; Cruz-Yusta, M.; Mármol, I.; Morales, J.; Vila, J.; Sánchez, L. Enhanced photocatalytic degradation of NO_x gases by regulating the microstructure of mortar cement modified with titanium dioxide. *Build. Environ.* **2013**, *69*, 55–63. [[CrossRef](#)]
4. Vulic, T.; Rudic, O.; Hadnadjev-Kostic, M.; Radeka, M.; Marinkovic-Neducin, R.; Ranogajec, J. Improvement of cement-based mortars by application of photocatalytic active Ti–Zn–Al nanocomposites. *Cem. Concr. Compos.* **2013**, *36*, 121–127. [[CrossRef](#)]
5. Macphee, D.; Folli, A. Photocatalytic concretes—The interface between photocatalysis and cement chemistry. *J. Cem. Concr. Res.* **2016**, *85*, 48–54. [[CrossRef](#)]
6. Zhang, R.; Cheng, X.; Hou, P.; Ye, Z. Influences of nano-TiO₂ on the properties of cement-based materials: Hydration and drying shrinkage. *Construct. Build. Mater.* **2015**, *81*, 35–41. [[CrossRef](#)]
7. Yousefi, A.; Allahverdi, A.; Hejazi, P. Effective dispersion of nano-TiO₂ powder for enhancement of photocatalytic properties in cement mixes. *Construct. Build. Mater.* **2013**, *41*, 224–230. [[CrossRef](#)]
8. Liu, P.; Gao, Y.; Wang, F.; Zhang, W.; Yang, L.; Yang, J.; Liu, Y. Photocatalytic activity of Portland cement loaded with 3D hierarchical Bi₂WO₆ microspheres under UV-visible light. *Construct. Build. Mater.* **2016**, *120*, 42–47. [[CrossRef](#)]
9. Wang, X.; Maeda, K.; Thomas, A.; Takanebe, K.; Xin, G.; Carlsson, J.M.; Domen, K.; Antonietti, M. A metal-free polymeric photocatalyst for hydrogen production from water under UV-visible light. *J. Nat. Mater.* **2009**, *8*, 76. [[CrossRef](#)]
10. Ong, W.J.; Tan, L.L.; Ng, Y.H.; Yong, S.T.; Chai, S.P. Graphitic carbon nitride (g-C₃N₄)-based photocatalysts for artificial photosynthesis and environmental remediation: Are we a step closer to achieving sustainability? *J. Chem. Rev.* **2016**, *116*, 7159–7329. [[CrossRef](#)]
11. Shalom, M.; Inal, S.; Fettkenhauer, C.; Neher, D.; Antonietti, M. Improving carbon nitride photocatalysis by supramolecular preorganization of monomers. *J. Am. Chem. Soc.* **2013**, *135*, 7118–7121. [[CrossRef](#)] [[PubMed](#)]
12. Mamba, G.; Mishra, A. Graphitic carbon nitride (g-C₃N₄) nanocomposites: A new and exciting generation of UV-visible light driven photocatalysts for environmental pollution remediation. *Appl. Catal. B Environ.* **2016**, *198*, 347–377. [[CrossRef](#)]
13. Guo, S.E.; Deng, Z.P.; Li, M.X.; Jiang, B.J.; Tian, C.G.; Pan, Q.J.; Fu, H.G. Phosphorus-Doped Carbon Nitride Tubes with a Layered Micro-nanostructure for Enhanced Visible-Light Photocatalytic Hydrogen Evolution. *J. Angew. Chem. Int. Ed.* **2016**, *55*, 1830–1834. [[CrossRef](#)] [[PubMed](#)]
14. Ge, L.; Han, C.C.; Liu, J.; Li, Y.F. Enhanced UV-visible light photocatalytic activity of novel polymeric g-C₃N₄ loaded with Ag nanoparticles. *J. Appl. Catal. A General.* **2011**, *409–410*, 215–222. [[CrossRef](#)]
15. Yuan, B.; Chu, Z.; Li, G.Y.; Jiang, Z.H.; Hu, T.J.; Wang, Q.H.; Wang, C.H. Water-soluble ribbon-like graphitic carbon nitride (g-C₃N₄): Green synthesis, self-assembly and unique optical properties. *J. Mater. Chem. C* **2014**, *2*, 8212–8215. [[CrossRef](#)]
16. Liu, W.; Wang, M.; Xu, C.; Chen, S.; Fu, X. Significantly enhanced visible-light photocatalytic activity of g-C₃N₄ via ZnO modification and the mechanism study. *J. Mol. Catal. A Chem.* **2013**, *368–369*, 9–15. [[CrossRef](#)]

17. Yang, N.; Li, G.; Wang, W.; Yang, X.; Zhang, W.F. Photophysical and enhanced daylight photocatalytic properties of N-doped TiO₂/g-C₃N₄ composites. *J. Phys. Chem. Solids* **2011**, *72*, 1319–1324. [[CrossRef](#)]
18. Peng, F.; Ni, Y.; Zhou, Q.; Kou, J.H.; Lu, C.H.; Xu, Z.Z. New g-C₃N₄ based photocatalytic cement with enhanced visible-light photocatalytic activity by constructing muscovite sheet/SnO₂ structures. *Construct. Build. Mater.* **2018**, *179*, 315–325. [[CrossRef](#)]
19. Parida, K.; Mohapatra, L. Recent progress in the development of carbonate-intercalated Zn/Cr LDH as a novel photocatalyst for hydrogen evolution aimed at the utilization of solar light. *Dalton Trans.* **2012**, *41*, 1173e8. [[CrossRef](#)]
20. Kumar, S.; Durrndell, L.J.; Manayil, J.C.; Isaacs, M.A.; Parlett, C.M.A.; Karthikeyan, S.; Douthwaite, R.E.; Coulson, B.; Wilson, K.; Lee, A.F. Delaminated CoAl-ayered double hydroxide@TiO₂ heterojunction nanocomposites for photocatalytic reduction of CO₂. *Part. Part. Syst. Charact.* **2017**, *35*, 1700317. [[CrossRef](#)]
21. Shao, M.; Ning, F.; Wei, M.; Evans, D.G.; Duan, X. Hierarchical Nanowire Arrays Based on ZnO Core -Layered Double Hydroxide Shell for Largely Enhanced Photoelectrochemical Water Splitting. *Adv. Funct. Mater.* **2014**, *24*, 580–586. [[CrossRef](#)]
22. Sun, Y.; Wang, L.; Wang, T.; Liu, X.; Li, C. Improved photocatalytic activity of Ni₂P/NiCo-LDH composites via a Co–P bond charge transfer channel to degrade tetracycline under UV-visible light. *J. Alloy. Compd.* **2021**, *852*, 156963. [[CrossRef](#)]
23. Yang, Z.; Fischer, H.; Polder, R. Modified Hydrotalcites as A New Emerging Class of Smart Additive of Reinforced Concrete for Anti-Corrosion Applications: A Literature Review. *Mater. Corros.* **2013**, *64*, 1066–1074. [[CrossRef](#)]
24. Yang, Z.; Fischer, H.; Polder, R. Synthesis and Characterisation of Modified Hydrotalcites and Their Ion Exchange Characteristics in Chloride-rich Simulated Concrete Pore Solution. *Cem. Concr. Compos.* **2014**, *47*, 87–93. [[CrossRef](#)]
25. Yang, Z.; Fischer, H.; Polder, R. Laboratory Investigation of the Influence of Two Types of Modified Hydrotalcites on Chloride Ingress into Cement Mortar. *Cem. Concr. Compos.* **2015**, *58*, 105–113. [[CrossRef](#)]
26. Li, H.; Li, J.; Xu, C.; Yang, P.; Ng, D.H.L.; Song, P.; Zuo, M. Hierarchically porous MoS₂/CoAl-LDH/HCF with synergistic adsorption photocatalytic performance under UV-visible light irradiation. *J. Alloys Compd.* **2017**, *698*, 852e62. [[CrossRef](#)]
27. Sanati, S.; Rezvani, Z. g-C₃N₄ nanosheet@CoAl-layered double hydroxide composites for electrochemical energy storage in supercapacitors. *J. Chem. Eng.* **2019**, *362*, 743–757. [[CrossRef](#)]
28. Tonda, S.; Kumar, S.; Bhardwaj, M.; Yadav, P.; Ogale, S. g-C₃N₄/NiAl-LDH 2D/2D hybrid heterojunction for high-performance photocatalytic reduction of CO₂ into renewable fuels. *ACS Appl. Mater. Interfaces* **2018**, *10*, 2667–2678. [[CrossRef](#)]
29. Liu, J.; Li, J.; Bing, X.; Ng, D.H.L.; Cui, X.L.; Ji, F.; Kionga, D.D. ZnCr-LDH/N-doped graphitic carbon incorporated g-C₃N₄ 2D/2D nanosheet heterojunction with enhanced charge transfer for photocatalysis. *J. Mater. Res. Bull.* **2018**, *102*, 379–390. [[CrossRef](#)]
30. Shi, J.; Li, S.; Wang, F.; Gao, L.N.; Li, Y.M.; Zhang, X.R.; Lu, J. 2D/2D g-C₃N₄/MgFe MMO nanosheets heterojunctions with enhanced visible-light photocatalytic H₂ production. *J. Alloys Compd.* **2018**, *769*, 611–619. [[CrossRef](#)]
31. Kaur, H.; Singh, S.; Pal, B. Freely standing MgAl-layered double hydroxides nanosheets and their derived metal oxides on g-C₃N₄ thin-layer designed for obtaining synergic effect of adsorption and photocatalysis. *J. Appl. Clay Sci.* **2019**, *178*, 105131. [[CrossRef](#)]
32. Liu, J.; Zhang, T.; Wang, Z.C. Simple pyrolysis of urea into graphitic carbon nitride with recyclable adsorption and photocatalytic activity. *J. Mater. Chem.* **2011**, *21*, 14398–14401. [[CrossRef](#)]
33. Zhao, Y.; Li, F.; Zhang, R.; Evans, D.G.; Duan, X. Preparation of Layered Double-Hydroxide Nanomaterials with a Uniform Crystallite Size Using a New Method Involving Separate Nucleation and Aging Steps. *J. Chem. Mater.* **2002**, *14*, 4286–4291. [[CrossRef](#)]
34. Lin, B.; An, H.; Yan, X.; Zhang, T.; Wei, J.; Yang, G. Fish-scale structured g-C₃N₄ nanosheet with unusual spatial electron transfer property for high-efficiency photocatalytic hydrogen evolution. *J. Appl. Catal. B Environ.* **2017**, *210*, 173–183. [[CrossRef](#)]
35. Zhou, Y.; Zhang, L.; Huang, W.; Kong, Q.; Fan, X.; Wang, M.; Shi, J. N-doped graphitic carbon-incorporated g-C₃N₄ for remarkably enhanced photocatalytic H₂ evolution under UV-visible light. *Carbon* **2016**, *99*, 111–117. [[CrossRef](#)]
36. Duan, H.Z.; Zeng, H.Y.; Xiao, H.M.; Chen, C.R.; Xiao, G.F.; Zhao, Q. Optimization of ammonia nitrogen removal by SO₄²⁻-intercalated hydrotalcite using response surface methodology. *J. RSC Adv.* **2016**, *6*, 48329–48335. [[CrossRef](#)]
37. Jo, W.K.; Tonda, S. Novel CoAl-LDH/g-C₃N₄/RGO ternary heterojunction with noTable 2D/2D/2D configuration for highly efficient visible-light-induced photocatalytic elimination of dye and antibiotic pollutants. *J. Hazard. Mater.* **2019**, *368*, 778–787. [[CrossRef](#)]
38. Tauc, J.; Grigorovici, R.; Vancu, A. Optical properties and electronic structure of amorphous Ge and Si. *J. Mat. Res. Bull.* **1968**, *3*, 37–46. [[CrossRef](#)]
39. Jo, W.K.; Kumar, S.; Yadav, P.; Tonda, S. In situ phase transformation synthesis of unique Janus Ag₂O/Ag₂CO₃ heterojunction photocatalyst with improved photocatalytic properties. *Appl. Surf. Sci.* **2018**, *445*, 555–562. [[CrossRef](#)]
40. Wang, Z.; Guan, W.; Sun, Y.; Dong, F.; Zhou, Y.; Ho, W.K. Water-assisted production of honeycomb-like g-C₃N₄ with ultralong carrier lifetime and outstanding photocatalytic activity. *Nanoscale* **2015**, *7*, 2471–2479. [[CrossRef](#)]
41. Yang, X.; Qian, F.; Zou, G.; Li, M.L.; Lu, J.R.; Li, Y.M.; Bao, M. Facile fabrication of acidified g-C₃N₄/g-C₃N₄ hybrids with enhanced photocatalysis performance under UV-visible light irradiation. *J. Appl. Catal. B Environ.* **2016**, *193*, 22–35. [[CrossRef](#)]
42. Guo, S.; Chi, L.; Zhao, T.; Nan, Y.B.; Sun, X.; Huang, Y.L.; Hou, B.R.; Wang, X.T. Construction of MOF/TiO₂ nanocomposites with efficient visible-light-driven photocathodic protection. *J. Electro. Chem.* **2021**, *880*, 114915. [[CrossRef](#)]
43. Van Pham, V.; Mai, D.Q.; Bui, D.P.; Man, T.V.; Zhu, B.C.; Zhang, L.Y.; Sangkawore, J.; Tantirungrotechai, J.; Reutrakul, V.; Cao, T.M. Emerging 2D/0D g-C₃N₄/SnO₂ S-scheme photocatalyst: New generation architectural structure of heterojunctions toward visible-light-driven NO degradation. *Environ. Pollut.* **2021**, *286*, 117510. [[CrossRef](#)] [[PubMed](#)]

44. Vinh, T.H.T.; Thi, C.M.; Van Viet, P. Enhancing photocatalysis of NO gas degradation over g-C₃N₄ modified α -Bi₂O₃ microrods composites under visible light. *Mater. Lett.* **2020**, *281*, 128637. [[CrossRef](#)]
45. Wang, M.; Tan, G.; Dang, M.; Wang, Y.; Zhang, B.X.; Ren, H.J.; Lv, L.; Xia, A. Dual defects and build-in electric field mediated direct Z-scheme W₁₈O₄₉/g-C₃N₄-x heterojunction for photocatalytic NO removal and organic pollutant degradation. *J. Colloid Interface Sci.* **2021**, *582*, 212–226. [[CrossRef](#)] [[PubMed](#)]
46. Lu, Z.Z.; Li, S.Q.; Xiao, J.Y. Synergetic Effect of Na–Ca for Enhanced Photocatalytic Performance in NO_x Degradation by g-C₃N₄. *Catal. Lett.* **2021**, *151*, 370–381. [[CrossRef](#)]
47. Luo, J.; Dong, G.; Zhu, Y.; Yang, Z.; Wang, C. Switching of semiconducting behavior from n-type to p-type induced high photocatalytic NO removal activity in g-C₃N₄. *Appl. Catal. B Environ.* **2017**, *214*, 46–56. [[CrossRef](#)]
48. Hu, J.; Chen, D.; Li, N.; Xu, Q.F.; Li, H.; He, J.H.; Lu, J.M. Fabrication of graphitic-C₃N₄ quantum dots/graphene-InVO₄ aerogel hybrids with enhanced photocatalytic NO removal under visible-light irradiation. *Appl. Catal. B Environ.* **2018**, *236*, 45–52. [[CrossRef](#)]
49. Ren, Y.; Li, Y.; Wu, X.; Wang, J.; Zhang, G. S-scheme Sb₂WO₆/g-C₃N₄ photocatalysts with enhanced visible-light-induced photocatalytic NO oxidation performance. *Chin. J. Catal.* **2021**, *42*, 69–77. [[CrossRef](#)]
50. Yang, L.; Wang, P.; Yin, J.; Wang, C.Y.; Dong, G.H.; Wang, Y.H.; Ho, W.K. Engineering of reduced graphene oxide on nanosheet-g-C₃N₄/perylene imide heterojunction for enhanced photocatalytic redox performance. *Appl. Catal. B Environ.* **2019**, *250*, 42–51. [[CrossRef](#)]
51. Zhou, Q. Preparation and Properties of Cementitious Carbon Nitride Composite Photocatalytic Materials. Master's Thesis, Nanjing University of Technology, Nanjing, China, 2017.
52. Pan, D.; Zhang, J.; Li, Z.; Wu, M.H. Hydrothermal route for cutting graphene sheets into blue-luminescent graphene quantum dots. *Adv. Mater.* **2010**, *22*, 734–738. [[CrossRef](#)] [[PubMed](#)]
53. Guo, J.; Qian, H.; Liu, P.F.; Ma, J.Y. Fabrication of durability superhydrophobic LDH coating on zinc sheet surface via NH₄F-assisted in-situ growth and post-modification for enhancing anti-corrosion and anti-icing. *Appl. Clay Sci.* **2019**, *180*, 105182. [[CrossRef](#)]
54. *Italian Standards UNI 11259:2008*; Determination of the Photocatalytic Activity of Hydraulic Binders-Rodammina Test Method. Ente Nazionale Italiano di Unificazione: Milan, Italy, 2008.
55. Gauvin, F.; Caprai, V.; Yu, Q.L.; Brouwers, H.J.H. Effect of the morphology and pore structure of porous building materials on photocatalytic oxidation of air pollutants. *J. Appl. Catal. B Environ.* **2018**, *227*, 123–131. [[CrossRef](#)]